catalysts

MDPI

Article

V_6O_{13} Micro-Flower Arrays Grown In Situ on Ni Foam as Efficient Electrocatalysts for Hydrogen Evolution at Large Current Densities

Yajie Xie [1], Jianfeng Huang [1,*], Yufei Wang [1], Liyun Cao [1], Yong Zhao [2], Koji Kajiyoshi [3], Yijun Liu [2] and Liangliang Feng [1,4,*]

[1] School of Material Science and Engineering, International S&T Cooperation Foundation of Shaanxi Province, Shaanxi University of Science and Technology, Xi'an 710021, China
[2] Guangdong Mona Lisa Group Co., Ltd., Foshan 528211, China
[3] Research Laboratory of Hydrothermal Chemistry, Kochi University, Kochi 780-8520, Japan
[4] Key Laboratory of Advanced Energy Materials Chemistry (Ministry of Education), Nankai University, Tianjin 300071, China
* Correspondence: huangjf@sust.edu.cn (J.H.); fengll@sust.edu.cn (L.F.)

Abstract: Developing a high-activity, robust and economic electrocatalyst for large-scale green hydrogen production is still of great significance. Herein, a novel V_6O_{13} nanosheets self-assembled micro-flower array self-supporting electrode is synthesized using a facile one-pot hydrothermal route. Owing to the large electrochemically active surface area of a unique hierarchical micro-flower and the stable all-in-one structure, the as-prepared V_6O_{13}/NF electrode delivers impressive HER activity with extremely low overpotentials of 125 and 298 mV at large current densities of 100 and 1000 mA cm^{-2}, respectively, and a long-term durability for at least 90 h in an alkaline condition. This work extends the application of vanadium oxides to the realm of electrocatalytic hydrogen fuel production.

Keywords: vanadium oxide; electrocatalysis; hydrogen evolution

check for updates

Citation: Xie, Y.; Huang, J.; Wang, Y.; Cao, L.; Zhao, Y.; Kajiyoshi, K.; Liu, Y.; Feng, L. V_6O_{13} Micro-Flower Arrays Grown In Situ on Ni Foam as Efficient Electrocatalysts for Hydrogen Evolution at Large Current Densities. *Catalysts* **2023**, *13*, 914. https://doi.org/10.3390/catal13050914

Academic Editor: Carlo Santoro

Received: 24 March 2023
Revised: 17 May 2023
Accepted: 18 May 2023
Published: 22 May 2023

1. Introduction

Developing renewable green energy that is eco-friendly and has high efficiency has become an irresistible trend and a global challenge because of the overconsumption of the fossil fuels and excessive CO_2 emissions [1,2]. Nowadays, water electrolysis technology is widely recognized as a promising sustainable pathway to obtain clean, high-purity and high-efficiency hydrogen energy [3,4]. Until now, Pt and Pt-based materials were identified as state-of-the art electrocatalysts that only need quite low potentials to overcome the activation of the energy barrier for a hydrogen evolution reaction (HER) [5,6]. Due to their expensive cost and rare global reserves restricting their wide applications, it is urgent to develop non-precious metal electrocatalysts for the HER of green H_2 production.

Transition metal vanadium-based compounds, including carbides, sulfides and nitrides of vanadium, have been widely investigated as non-noble metal electrocatalysts due to the multivalent states of V metal, its low-cost position and metallic nature [7–9]. Among them, the vanadium oxide family includes V_2O_5, VO_2, V_2O_3, V_6O_{13} and so on, and exhibits excellent electrochemical properties and rich active sites [10–13]. Zhang et al. constructed oxygen vacancy (O_V) to obtain a higher valence electron binding energy for the regulation of surface chemical states, leading to moderating the adsorption of H* at the V center, and thus optimizing V_2O_5 electrocatalytic activity and stability [14]. The oxygen evolution activity of VO_2 was studied by Yun-Hyuk Choi, proving that the performance of V^{4+} was more favorable to the OER catalysis than that of V^{5+} [15]. Ding et al. reported on the fabrication of 3D V_6O_{13} nanotextiles as cathodes of lithium-ion batteries, exhibiting outstanding Li^+ storage properties such as excellent rate capability, high capacity and

stable cyclability [16]. Rao et al. proposed a V_2O_3-based hybrid electrocatalyst for a highly efficient bifunctional air electrode of a Zn–air battery with good cycling stability and mechanical flexibility [17]. Some research groups made great efforts on the OER activity and battery performance, while the performance of vanadium oxide in electrocatalytic hydrogen evolution is a big challenge that still requires more effort for boosting the electrocatalytic HER performance [18–21].

In this work, we report on the synthesis of a V_6O_{13} nanosheets self-assembled micro-flower array grown in situ on Ni foam as a highly active and stable HER electrocatalyst at large current densities using a facile one-step hydrothermal method. Benefiting from the well-integrated nanoarray structure, the precise control of the vanadium source content and appropriate oxalic acid addition, the electron and charges transport rate were well motivated, the HER kinetics were accelerated and numerous exposed catalytic active sites were enlarged, thus the resulting V_6O_{13}/NF displayed a glorious HER performance at the large current densities of 100 mA cm^{-2} and 1000 mA cm^{-2} with an extremely low overpotential of 125 mV and 298 mV, as well as a superior durability for at least 90 h in an alkaline condition. More broadly, these findings inspire new insights into the design of remarkable vanadium oxide electrocatalysts for efficient hydrogen production in the future.

2. Results

2.1. Structural and Morphological Characterizations

The V_6O_{13} nanosheets self-assembled micro-flower arrays grown in situ on nickel foam (denoted as V_6O_{13}/NF) were synthesized using a simple one-pot hydrothermal reaction, as illustrated in Figure 1. For comparative studies, a control sample was obtained under identical experimental conditions with the exception that no oxalic acid was added (denoted as VO_x/NF, Figure S1). As shown in Figure 2, the composition and crystal structure of the V_6O_{13}/NF materials scraped from NF were studied using X-ray diffraction (XRD). The obvious diffraction peaks were located at 25.4°, 26.8°, 30.1°, 33.5°, 45.6°, 45.8°, 49.5° and 59.8° and were attributed to (110), (003), (−401), (−311), (−601), (114), (020) and (−711) planes of the monoclinic V_6O_{13} phase (PDF #89-0100), respectively. The results manifest that V_6O_{13} was successfully synthesized on the surface of the NF substrate. For comparison, the VO_X/NF sample was obtained when $H_2C_2O_4$ was not added into the synthetic process. As shown in Figure S2A, it can be observed that some diffraction peaks located at 21.55°, 27.68° and 35.45°are indexed to (200), (202) and (311) crystal planes of the tetragonal V_4O_9 (PDF#23-0720) phase, and other diffraction peaks at 20.26°, 26.13° and 31.00° can be assigned to (001), (110) and (400) planes of orthorhombic V_2O_5 (PDF#41-1426). The results confirm that the existence of $H_2C_2O_4$ played an important role in the formation of the V_6O_{13} phase.

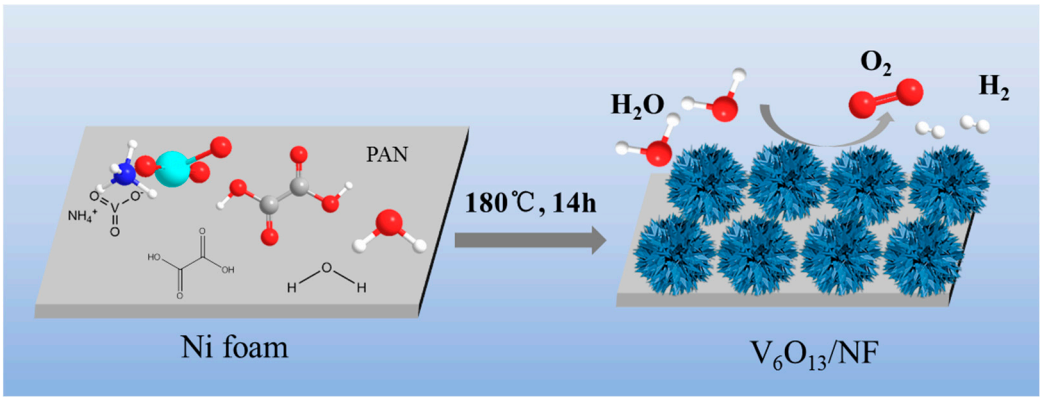

Figure 1. Synthetic strategy and schematic illustration of the construction of V_6O_{13}/NF.

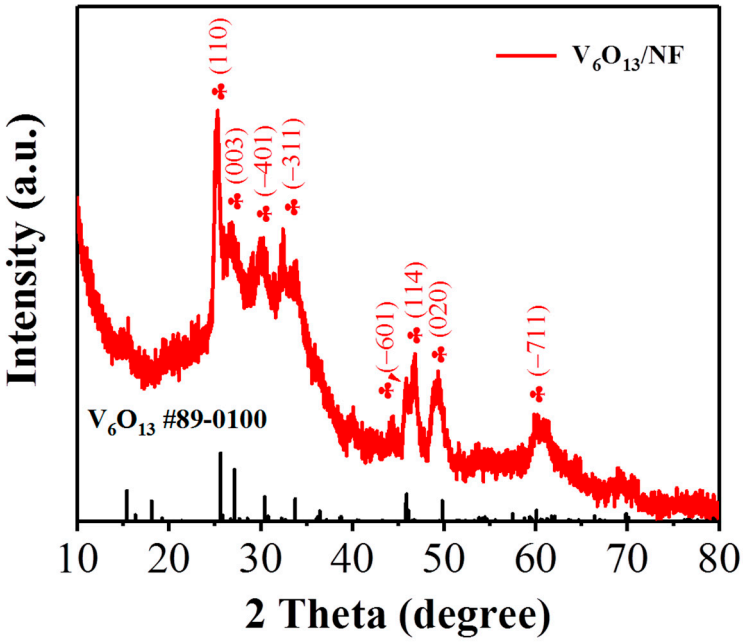

Figure 2. XRD pattern of V_6O_{13}/NF.

Then, scanning electron microscopy (SEM) images were conducted to investigate the microstructure and morphology characteristics of the synthetic sample. Firstly, to investigate the effects of the content of the V source on the morphology of V_6O_{13}, three more samples were prepared by changing the addition of NH_4VO_3 (0.2, 0.5 and 1.0 g), denoted as sample-0.2 g, sample-1.0 g, and the remarkable as-prepared V_6O_{13}/NF, here denoted as sample-0.5 g. The SEM spectrum of sample-0.2 g indicated that a few nanosheets and agglomeration were formed on the surface of the NF and the self-assembly micro-flower arrays were not formed when there was not enough of NH_4VO_3 content (Figure 3A,B). As displayed in Figure 3C, the entire NF substrate of sample-0.5 g is equally and densely covered by the micro-flower arrays self-assembled with the V_6O_{13} nanosheets. The magnificated SEM view in Figure 3D reveals that the structure of every micro-flower is formed by dense nanosheets stretching outward. It is speculated that with the increasing amount of the vanadium source, the much larger diameter of the nanosheets in sample-1.0 g evenly grows on the surface of the nickel foam. The sheets with micrometer scale will extend the charge transfer path and reduce the exposed electrochemical active area, which is not conducive to the hydrogen evolution reaction kinetics and efficient electrocatalytic activity (Figure 3E,F). Combined with the SEM images (Figure 3C,D), the V_6O_{13}/NF micro-flower array with the shape of a globular peony structure possesses smaller nanosheets, more accessible active sites and consequently facilitates the faster electrolyte and electron transportation, thus improving the catalytic HER performance [22,23].

Moreover, the transmission electron microscopy (TEM) image (Figure 4A) of V_6O_{13}/NF shows that the micro-flower array consisting of a nanosheet structure corresponds to its SEM results (Figure S2C). The HRTEM (Figure 4B) image of V_6O_{13}/NF displays distinct lattice fringes with a distance of 0.198 nm, which can be attributed to the (−601) crystal plane of V_6O_{13}. Furthermore, the selected area for the electron diffraction (SAED) pattern of V_6O_{13}/NF in Figure 4C shows a series of concentric rings, confirming its high crystallinity, which well coincides with the (110) and (020) plane of V_6O_{13}. The EDS mapping further confirms that V, O and Ni elements are homogeneously distributed over the whole V_6O_{13}/NF nanosheet (Figure 4D–G). According to Figure S2B–H, the micro-morphology and element composition of VO_X/NF are also observed. The SEM of VO_X/NF in Figure S2B and the insert image indicate that the size of the VO_X/NF nanosheets is much larger than that of V_6O_{13}/NF, and these nanosheets self-assemble into larger micron-flowers. Obviously, a too large size is not conducive to the efficient electrocatalytic reaction [24]. The

TEM and HRTEM images show the clear lattice fringes with a crystal spacing of 0.199 nm corresponding to the (411) crystal plane of V_2O_5. The SAED pattern in Figure S2D inset exhibits the crystal plane composed of bright diffraction points, demonstrating the single crystal nature of VO_X/NF, which is attributed to the (200) and (110) planes of V_2O_5 and (200) plane of V_4O_9, and is consistent with the XRD result in Figure S2A. Combined with the corresponding EDS mapping (Figure S2E–H), it can be observed that the elements of V, O and Ni are uniformly dispersed in the VO_X/NF nanosheet.

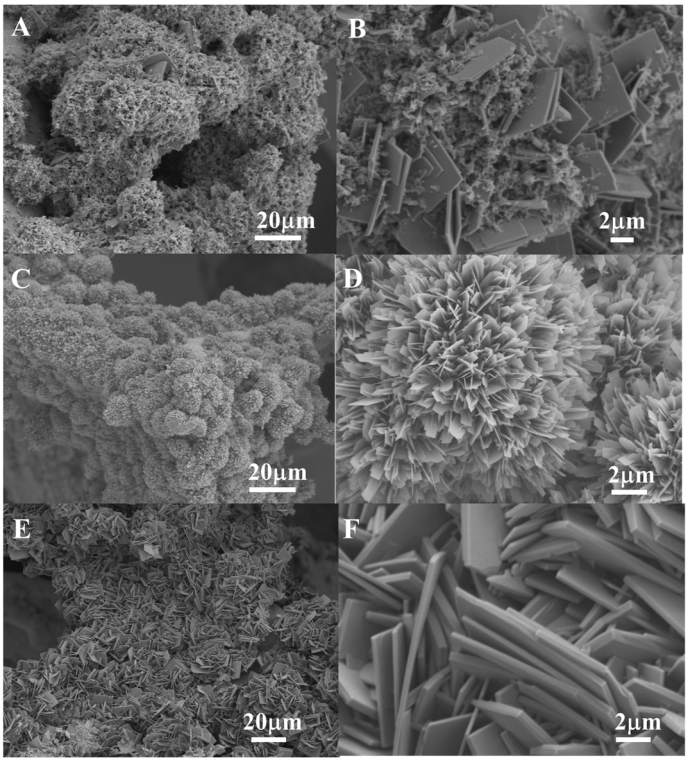

Figure 3. SEM images of (**A**,**B**) sample-0.2 g; (**C**,**D**) sample-0.5 g; and (**E**,**F**) sample-1.0 g.

X-ray photoelectron spectroscopy (XPS) measurement was performed to investigate the surface chemical composition and the electronic states of V_6O_{13}/NF and VO_X/NF. As indicated in Figure 5A, the survey XPS spectrum of V_6O_{13}/NF and VO_X/NF, the elemental peaks for Ni, O and V are observed. The high-resolution XPS spectra of O 1s in V_6O_{13}/NF can be resolved into three obvious peaks at 529.80 eV, 530.93 eV and 533.22 eV (Figure 5B), which are, respectively, belonging to the metal oxygen (M–O), hydroxyl oxide (OH^-), and adsorbed oxygen (H_2O) [25,26]. Correspondingly, the M–O peak of O 1s region in V_6O_{13}/NF exhibits a slight positive shift of ~0.07 eV relative to that of VO_X/NF, and the relative intensity of the M–O peak in V_6O_{13}/NF is marginally higher than that of VO_X/NF, indicating that the V–O covalent bond in V_6O_{13}/NF is stronger, which is more conducive to increase the electron transfer rate, thus enhancing the capability of electron donation. The hydroxyl oxide in O 1s of V_6O_{13}/NF is slightly shifted by 0.03 eV to the positive binding energy as compared to VO_X/NF, and the relative intensity of adsorbed oxygen deriving from O 1s peak in V_6O_{13}/NF is greater than that of VO_X/NF, suggesting that the introduction of $H_2C_2O_4$ effectively accelerated the water decomposition process, providing more adequate contact between the electrode and electrolyte in the catalytic reaction.

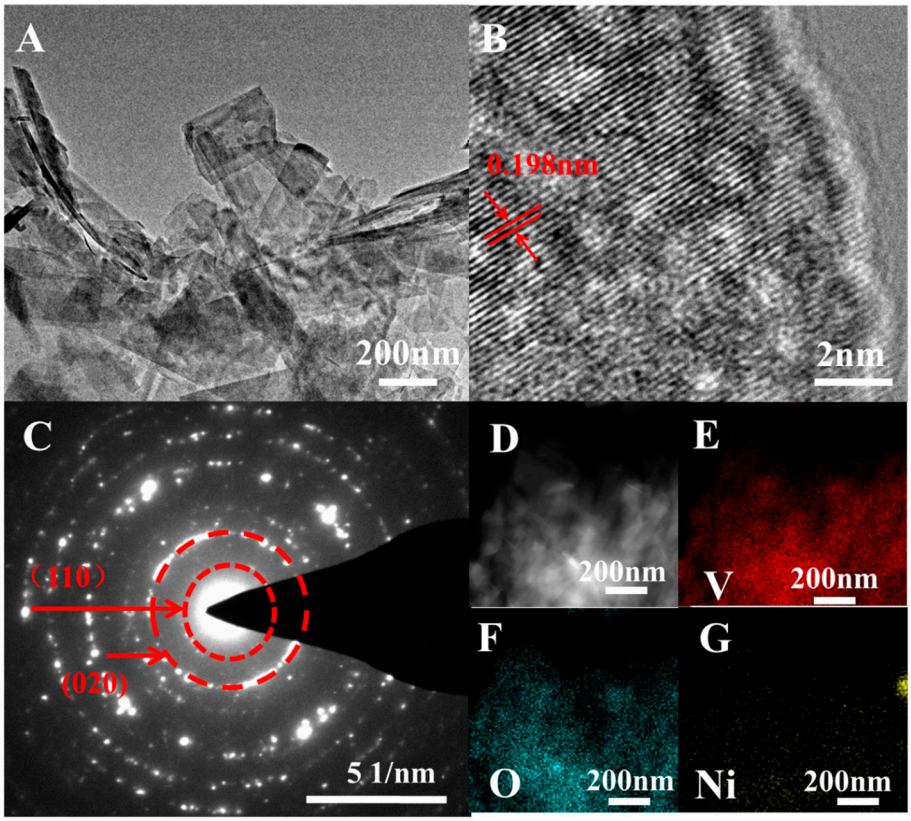

Figure 4. (**A**) TEM image of V_6O_{13}/NF; (**B**) HRTEM image of V_6O_{13}/NF; (**C**) SAED pattern; and (**D**–**G**) aberration-corrected TEM image and the corresponding elemental mapping images of V_6O_{13}/NF.

As shown in Figure 5C, a close inspection discloses that the XPS spectra of Ni 2p and the Ni 2p spectra of V_6O_{13}/NF and VO_X/NF all exhibited two primary peaks: Ni $2p_{1/2}$ (865–885 eV) and Ni $2p_{3/2}$ (850–865 eV), originating from the spin–orbit splitting of Ni [27]. There are three peaks located at 852.20 eV, 854.42 eV and 859.18 eV, respectively, belonging to the Ni $2p_{3/2}$ peaks of Ni^{2+}, Ni^{3+} and the corresponding satellite peak in V_6O_{13}/NF. The peaks located at 869.58 eV, 872.60 eV and 880.15 eV ascribe to the Ni $2p_{1/2}$ of Ni^{2+}, Ni^{3+} and accompany satellite peaks in VO_X/NF [28]. The peaks located at 852.22 eV, 854.74 eV and 860.76 eV are assigned to Ni^{2+}, Ni^{3+} and the shakeup satellite peak of Ni $2p_{3/2}$ in VO_X/NF, respectively. Wherein three components are recognized at 869.34 eV, 872.52 eV and 880.10 eV belonged to Ni $2p_{1/2}$ of VO_X/NF. It is obvious that the peak positions of Ni 2p in V_6O_{13}/NF slightly shifted (~0.39 eV) towards a lower binding energy direction compared with that of VO_X/NF, indicating that the electrons of Ni transferred to the other atoms may be due to the addition of oxalic acid that oxidizes part of the Ni atom.

Similarly, the V 2p spectrum also had two modes including V $2p_{3/2}$ and V $2p_{1/2}$. As shown in Figure 5D, V_6O_{13}/NF displays four well-fitted peaks of V $2p_{3/2}$ focusing on 513.99 eV, 515.10 eV, 516.25 eV and 516.95 eV, respectively, and are assigned to V^{2+}, V^{3+}, V^{4+} and V^{5+}, and the characteristic peaks at 521.65 eV, 522.75 eV and 523.94 eV binding energy belong to V^{2+}, V^{3+} and V^{4+} [29]. Interestingly, vanadium in VO_X/NF only has three valence states, the corresponding peak positions are located at 513.58 eV, 514.79 eV and 515.85 eV, respectively, and are assigned to V^{2+}, V^{3+} and V^{4+}. An extra V^{5+} appearing in V_6O_{13}/NF compared to VO_X/NF may be due to the air oxidation [30]. V_2O_5 and V_4O_9 have higher valence states of vanadium as +5 and +4.5 than +4.33 of V_6O_{13}. It might be reasonable to suppose that oxalic acid is a key raw material for the synthesis of V_6O_{13} because of the fact that V_2O_5 and V_4O_9 have been reduced to V_6O_{13} by oxalic acid with expecting reactions, $V_2O_5 + x\ HCO_{2-} > V_2O_{5-x/2} + x/2\ H_2O + x\ CO_2$. The peak positions of V 2p in V_6O_{13}/NF were slightly positively shifted relative to VO_X/NF, combined with the peak position of O

1s negative shift, which means the electrons were transferred from V to O when V_6O_{13} was synthesized. The above results indicated that the construction of V_6O_{13} nanoarchitecture changes the valence state of the V element, regulates the electron structure and promotes the electron transfer between V, O and Ni, eventually accelerating the reaction kinetics of HER with an enhanced catalytic activity.

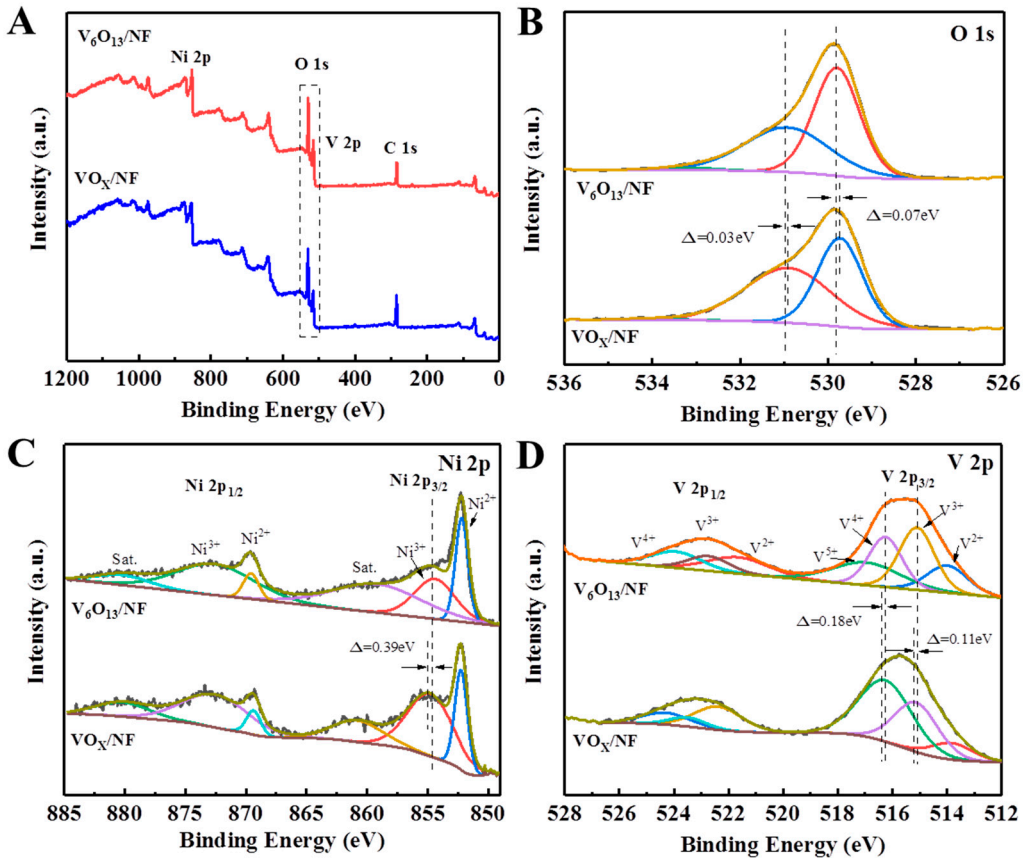

Figure 5. High-resolution XPS spectra: (**A**) survey; (**B**) O 1s; (**C**) Ni 2p; and (**D**) V 2p of V_6O_{13}/NF and VO_X/NF.S.

2.2. Electrocatalytic HER Performance of the as-Synthesized Catalysts

The HER performance of V_6O_{13}/NF was conducted using a standard three-electrode system in 1 M KOH solution to evaluate the electrocatalytic activity. Here, the binder-free self-supporting electrodes were used directly as the working electrodes with the same exposed electrocatalytic area (the details of the experiment concerning the HER measurements are described in the following Section 3.5). Firstly, to investigate the effect of different contents of the vanadium source on the HER performance of V_6O_{13}/NF, sample-0.2 g, sample-0.5 g and sample-1.0 g were prepared by changing the amount of NH_4VO_3 (0.2, 0.5 and 1.0 g), respectively, and the contrast LSV curve is shown in Figure S3. The result reveals that sample-0.5 g (V_6O_{13}/NF) shows the best HER performance, indicating that the amount of NH_4VO_3 has a significant effect on the catalytic HER activity performance. Combined with the SEM results of sample-0.2 g, sample-0.5 g and sample-1.0 g in Figure 3, the experimental results concluded that regulating the amount of the vanadium source can adjust the morphology and seriously affect the electrocatalytic hydrogen evolution performance. Furthermore, the XPS spectra of sample-0.2 g, sample-0.5 g and sample-1.0 g are displayed in Figure S4, and it can be clearly seen that the V peaks move positively towards the direction of high binding energy, while the Ni and O peaks shift negatively, indicating that more and more electrons are transferred from V to Ni and O when the

content of NH_4VO_3 is increased, which is further demonstrated by the amount of the V source that can regulate the electronic structure.

In order to further explore the hydrogen evolution performance of the as-prepared materials, the blank nickel foam (NF), V_6O_{13}/NF, VO_X/NF and commercial 25 wt% Pt/C/NF were compared in identical conditions. Figure 6A records the linear sweep voltammetry (LSV) with *iR*-correction of all samples. The V_6O_{13}/NF displays optimal HER activity, achieving large current densities of 100, 500 and 1000 mA cm^{-2} at a quite low overpotential of 125 mV, 228 mV and 298 mV, respectively, which are superior to the counterparts, such as VO_X/NF (155 mV, 268 mV and 362 mV) and NF (169 mV, 297 mV and 419 mV), ranking in first place among the reported vanadium oxide catalysts for the HER performance (Table S1) [31–33], and benefiting from the synergistic effect between exotic oxalic acid and V, O and Ni at optimum conditions. In particular, according to the LSV polarization curves, the HER activity of V_6O_{13}/NF manifests even better than that of 25 wt% Pt/C/NF commercial electrode in electrocatalytic activity at the large current of 1000 mA cm^{-2} (46 mV for 100 mA cm^{-2}, 190 mV for 500 mA cm^{-2}, 331 mV for 1000 mA cm^{-2}). In addition, the Tafel plots were fitted from the LSV curves to reveal the fast HER kinetics toward the various electrodes. According to Figure 6B, the Tafel slope of V_6O_{13}/NF, VO_X/NF, NF and commercial 25 wt% Pt/C/NF are displayed, the value of the Tafel slope in V_6O_{13}/NF (93 mV/dec) is much smaller than that of VO_X/NF (122 mV/dec) and the blank NF (159 mV/dec). In alkaline environments, when the Tafel slope is less than 120 mV/dec, the Volmer step mainly determines the rate of hydrogen evolution, indicating that V_6O_{13}/NF electrode firstly involves H^+ adsorption behavior in the HER process, resulting in V_6O_{13}/NF possessing the most active HER process among them [34,35].

Figure 6C shows the multi-step chronoamperometric curve for V_6O_{13}/NF to evaluate the HER stability from 50 mV to 500 mV of the overpotential, and each gradient lasts for 500 s. The result verifies that in the whole test range, the current density remains high in durability, which can be further validated by the LSV polarization curve in Figure 6D. Obviously, after continuously working for 90 h in an alkaline condition, the polarization curve of V_6O_{13}/NF displays an ignorable loss for the cathode current and there is only an unremarkable change. Moreover, V_6O_{13}/NF exhibits long-time electrocatalytic stability at 50 mA cm^{-2} current density without marked fluctuation over 90 h, wherein the electrode exhibited outstanding durability in Figure 6E.

Furthermore, the electrochemically active surface area (ECSA) is another evaluation index to assess the electrocatalytic activity, and the cyclic voltammogram (CV) curves (Figure S5) of V_6O_{13}/NF and VO_x/NF were recorded to evaluate the ECSA, which was correlated with the electrochemical double-layer capacitance (C_{dl}). The C_{dl} value could be linearly fitted from the corresponding CV, which was recorded at different scan rates from 20 to 120 mV/s. According to Figure 7A, the C_{dl} values of NF, VO_X/NF and V_6O_{13}/NF are quite different, in which the C_{dl} values of V_6O_{13}/NF are calculated to be 7.14 mF cm^{-2}, which is larger than that of VO_X/NF (2.65 mF cm^{-2}) and pure NF (0.53 mF cm^{-2}), respectively, indicating that the V_6O_{13}/NF exposes more electrocatalytic active sites. Then, the electrochemical impedance spectroscopy (EIS) results in Figure 7B verify that the V_6O_{13}/NF possesses the smaller semicircle dimension relative to VO_X/NF and NF electrodes, suggesting that it has relatively low charge transfer resistance (R_{ct}). Based on the fitted equivalent circuit inset in Figure 7B, the charge transfer resistance (R_{ct}) is fitted from the Nyquist plot in Table S2, and the values for V_6O_{13}/NF are calculated to be lower (1.819 Ω) than those for VO_X/NF (2.067 Ω) and NF (6.101 Ω), suggesting that V_6O_{13}/NF is beneficial to speed up the electron transport and HER kinetics. The results above suggested that V_6O_{13}/NF electrocatalysts were more efficient in the aggrandizement of catalytic reactive sites, favoring the Volmer-Heyrovsky step, thus enhancing the HER electrocatalytic performance. Therefore, the experimental results displayed the appropriate vanadium source content and oxalic acid addition could boost the electron transport rate, accelerate the HER reaction kinetics and expose numerous catalytic active sites, thus enhancing the HER electrocatalytic performance of V_6O_{13}/NF [36].

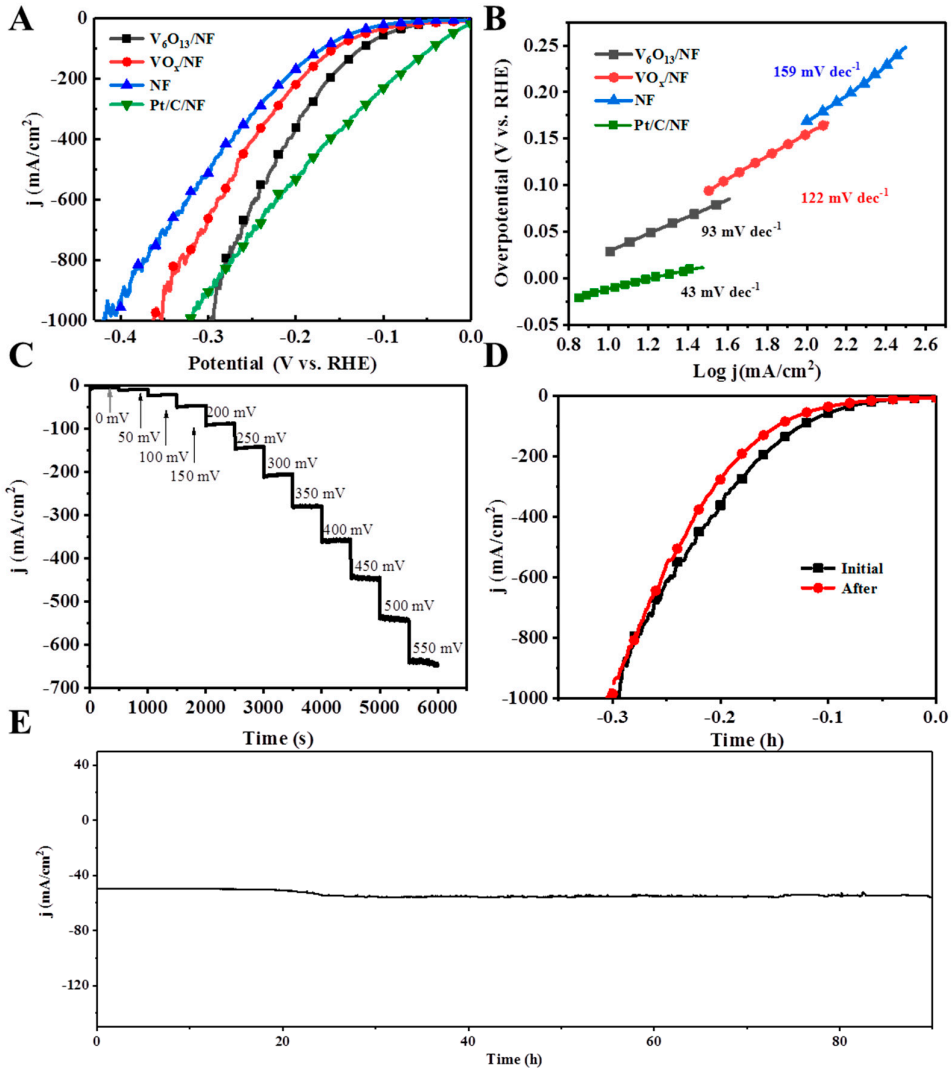

Figure 6. (**A**) HER polarization curves and (**B**) Tafel slopes of NF, V_6O_{13}/NF and VO_X/NF; (**C**) multi-step chronoamperometric curves of HER over V_6O_{13}/NF in 1.0 M KOH solution; (**D**) polarization curves recorded for V_6O_{13}/NF before and after the 90 h I-t test; and (**E**) I-t curve obtained for HER of V_6O_{13}/NF in 1.0 M KOH at a constant current density of 50 mA cm^{-2}.

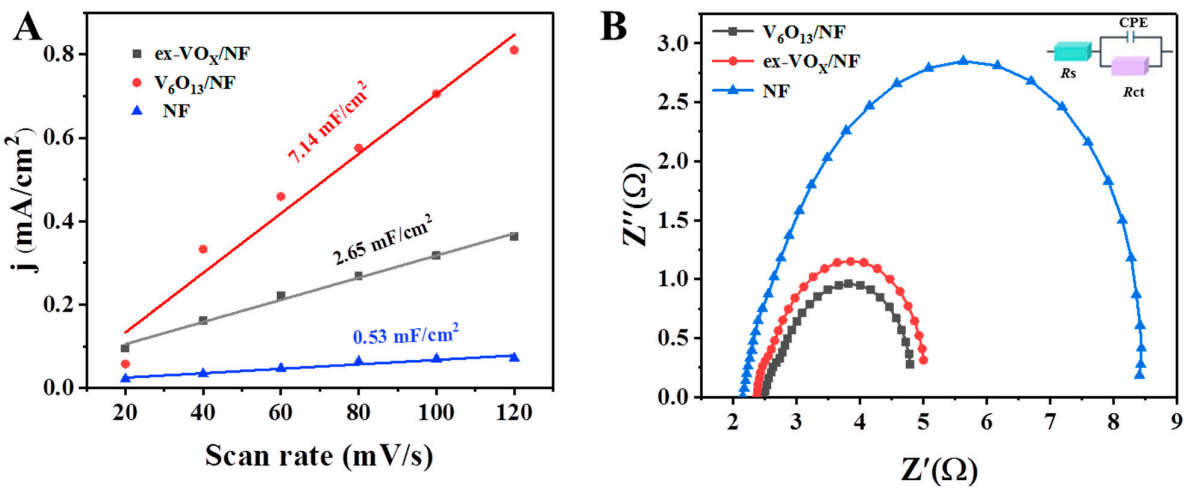

Figure 7. (**A**) Double-layer capacitance (C_{dl}) for the evaluation of ECSA and (**B**) Nyquist plots recorded at an overpotential of 50 mV of NF, V_6O_{13}/NF and VO_X/NF.

3. Materials and Methods

3.1. Chemicals and Reagents

All chemicals and reagents used in this work, including ammonium metavanadate (NH_4VO_3), polyaniline (PAN), oxalic acid ($H_2C_2O_4$) and potassium hydroxide (KOH), were purchased from Sinopharm Chemical Reagent Co., Ltd. (Beijing, China). without further purification treatment. Nickel foam (NF, 1.5 mm of thickness, 0.23 g cm^{-3} of density) was available from Suzhou Jiashide metal foam Co., Ltd. (Suzhou, China). The deionized water (18.25 M Ω of resistivity) was purified through the PALL PURELAB system (Beijing, China). NF (Nickel foam) was cut into a rectangle of 1 × 5 cm^2 and immersed in 3 mol L^{-1} hydrochloric acid and acetone for ultrasonic cleaning for 10 min. Finally, the foam was washed alternately with ethanol and deionized water several times, then dried under vacuum for 6 h at 40 °C for pretreatment to ensure that the organics and impurities were removed.

3.2. Synthesis of V_6O_{13}/NF

In this work, V_6O_{13}/NF was synthesized using a facile one-step hydrothermal method with 0.5 g of NH_4VO_3, 0.5 g of polyaniline (PAN) and 0.1 g of oxalic acid ($H_2C_2O_4$) dissolved in 30 mL ultrapure water, after magnetic stirring for 30 min; then, the cleaned nickel foam was added. Next, the above solution was loaded into the 50 mL high-pressure reaction kettle and heated at 180 °C for 14 h. Once cooled down to room temperature, the composite covering on the NF surface was produced, carefully cleaned alternately with ultrapure water and ethanol several times, and then dried in a vacuum for 10 h. Then, V_6O_{13}/NF self-supporting electrodes were obtained (as shown in Figure 1).

3.3. Synthesis of VOx/NF

The synthetic strategy of VO_X/NF was similar to that of V_6O_{13}/NF (0.5 g of NH_4VO_3, 0.5 g of polyaniline (PAN), except for removing $H_2C_2O_4$ in the synthetic process.

3.4. Synthesis of Sample-0.2 g, Sample-0.5 g and Sample-1.0 g

To investigate the effects of the content of the V source on V_6O_{13}, three more samples were prepared by changing the addition of NH_4VO_3 (0.2, 0.5 and 1.0 g), denoted as sample-0.2 g, sample-1.0 g and the remarkable as-prepared V_6O_{13}/NF, here denoted as sample-0.5 g, respectively.

3.5. General Characterizations

X-ray diffraction (XRD, D/max2200 V) data were recorded to analyze the phase and crystal texture of the samples with Cu Kα radiation (λ = 0.15406 nm). During the XRD test, the test angle was set to 10~80° and the scanning speed was set to 5°/min. In order to ensure the accuracy of the results, the self-supporting film material (VO_X/NF) was pressed flat before the test, and the powder material (V_6O_{13}/NF) was ground for refinement. The test results were analyzed and processed using MDI Jade 6.0 and Diamond software. Field emission scanning electron microscopy (FESEM, S4800, Hitachi, Tokyo, Japan) was performed to analyze the surface morphologies and nanostructure characteristics. Prior to testing, the self-supporting electrode samples were pasted to the conductive glue for observation. Transmission electron microscopy (TEM, Tecnai G2 F20S-TWIN, Tokyo, Japan) was employed to characterize the microstructure and morphologies. Prior to taking the TEM measurements, the samples were dissolved and dispersed in ethanol solution through ultrasound, then the liquid was dropped on the micro-grid and dried at room temperature. The elemental chemical compositions and bonding configuration were analyzed using an X-ray photoelectron spectrometer (XPS) (Thermo Fisher Scientific ESCALAB 250Xi, Waltham, MA, USA) with Al Kα radiation.

3.6. Electrochemical Tests

In this work, all electrochemical tests were measured using a three-electrode system on a CHI electrochemical workstation (ChenHua Instrument, Inc., Shanghai, China, CHI 660E). The as-prepared self-supporting electrode with a test surface area of 0.20 cm^2, carbon rod and $Hg/HgCl_2$ saturated calomel electrode were, respectively, employed as the working electrode, counter electrode and reference electrode, and were immersed in 1.0 M KOH during measurement. Following measurement, the load of V_6O_{13}/NF, as the working electrode, was 7 mg/cm^2 with a test surface area of 0.20 cm^2. Therefore, as the contrast working electrode, 1.41 mg of commercial 25 wt% Pt/C should have been dissolved in the mixed solution of isopropanol and Nafion, the mixed solution was ultrasonically and evenly coated on the NF work electrode surface, then the commercial 25 wt% Pt/C/NF was prepared. All of the potentials were converted to the reversible hydrogen electrode (RHE) as a reference based on the classical Nernst equation (E (RHE) = E ($Hg/HgCl_2$) + 0.0591 × pH + 0.2415). The polarization curves were recorded based on linear sweep voltammetry at the scanning rate of 5 mV s^{-1} with 85% *iR*-correction. The electrochemical impedance spectroscopy (EIS) was performed with an overpotential of 100 mV when the frequency scope ranged from 0.01 Hz to 1×10^5 Hz. Electrochemical active surface areas (ECSAs) were converted from collecting cyclic voltammetry (CV) at different scanning rates (20 mV s^{-1}, 40 mV s^{-1}, 60 mV s^{-1}, 80 mV s^{-1}, 100 mV s^{-1} and 120 mV s^{-1}) in the non-Faraday zone. The double-layer capacitance (C_{dl}) was evaluated at the potential −0.95 V. The electrochemical stability of the synthetic material was estimated at a galvanostatic measurement at a current density of 100 mA cm^{-2}.

4. Conclusions

In summary, a novel V_6O_{13}/NF nanosheets self-assembled micro-flower array grown in situ on nickel foam was successfully synthesized using a facile one-step hydrothermal method. V_6O_{13}/NF showed excellent performance of electrocatalytic HER activity at the large current density of 100 mA cm^{-2} with a considerably low overpotential of 125 mV and a small Tafel slope (93 mV dec^{-1}) as well as a superior HER catalytic stability for at least 90 h. Even more, at the larger current density of 1000 mA cm^{-2}, the overpotential was only 298 mV, which was superior to the commercial Pt/C/NF electrodes and most recently reported vanadium oxide materials. The highly efficient hydrogen evolution performance benefited from the unique hierarchical micro-flower, the stable well-integrated nanoarray structure and the precise control of vanadium source content, as well as from the appropriate oxalic acid addition that motivated the electron and charge transport rate, accelerated the HER reaction kinetics and enlarged the numerous exposed active catalytic sites, thus enhancing the HER electrocatalytic performance of V_6O_{13}/NF. The work we reported here on modulating the morphological and electronic structure extends the application of vanadium oxides as highly efficient electrocatalysts in the energy conversion and storage fields.

Supplementary Materials: The following supporting information can be downloaded at: https://www.mdpi.com/article/10.3390/catal13050914/s1, Figure S1: Synthetic strategy and schematic illustration of the construction of VO_X/NF; Figure S2: (A) XRD pattern of the as-synthesized VO_X/NF; (B,C) SEM and TEM images of the VO_X/NF nanosheets grown on NF substrate with different magnifications; (D) HRTEM image of VO_X/NF, with SAED pattern shown in the inset; and (E–H) TEM image and the corresponding elemental mapping images of VO_X/NF. Figure S3: HER LSV curves of sample-0.2, sample-0.5 and sample-1.0. Figure S4: XPS spectra of (A) sample-0.2 g, (B) sample-0.5 g and (C) sample-1.0 g for HER. Figure S5: CV curves of V6O13/NF (A) and VOX/NF (B). Table S1: Comparison of the electrocatalytic activity of V_6O_{13}/NF with previously reported vanadium oxide electrocatalysts. Table S2: Fitted data from Nyquist plots of the as-synthesized samples in the electrocatalytic HER test.

Author Contributions: Conceptualization, J.H., L.C. and L.F.; conceived the experiments, Y.X.; performed the major experiments and wrote the manuscript, Y.X.; performed a part of the measurements, Y.X., Y.W. and Y.Z.; review & editing, Y.X., K.K. and Y.L. All authors have read and agreed to the published version of the manuscript.

Funding: This research was funded by the National Natural Science Foundation of China (Grant No. 22179074, 52073166, 52172049, U22A20144), Scientific Research Project of the Education Department of Shaanxi Province (22JK0297), the Key Program for International S&T Cooperation Projects of Shaanxi Province (2020GHJD-04, 2023GHZD-08), Science and Technology Resource Sharing Platform of Shaanxi Province (2020PT-022); Agricultural Science and Technology Innovation Drive project of Shaanxi Agricultural Department (NYKJ-2022-XA-08).

Data Availability Statement: Not applicable.

Conflicts of Interest: The authors declare no conflict of interest.

References

1. Huang, H.; Yan, M. Graphene nanoarchitectonics: Recent advances in graphene-based electrocatalysts for hydrogen evolution reaction. *Adv. Mater.* **2019**, *31*, 1903415. [CrossRef] [PubMed]
2. Gao, L.; Zhong, X.; Chen, J.; Zhang, Y.; Liu, J.; Zhang, B. Optimizing the electronic structure of Fe-doped Co_3O_4 supported Ru catalyst via metal-support interaction boosting oxygen evolution reaction and hydrogen evolution reaction. *Chin. Chem. Lett.* **2022**, 108085. [CrossRef]
3. Huang, Q.; Liu, X.; Zhang, Z.; Wang, L.; Xiao, B. Dopant-vacancy activated tetragonal transition metal selenide for hydrogen evolution electrocatalysis. *Chin. Chem. Lett.* **2023**, *34*, 108046. [CrossRef]
4. Sreekanth, T.; Tamilselvan, M.; Yoo, K.; Kim, J. Microwave-assisted in situ growth of VO_2 nanoribbons on Ni foam as inexpensive bifunctional electrocatalysts for the methanol oxidation and oxygen evolution reactions. *Appl. Surf. Sci.* **2022**, *570*, 151119. [CrossRef]
5. He, J.; Liu, F.; Chen, Y.; Liu, X.; Zhang, X.; Zhao, L.; Chang, B.; Wang, J.; Liu, H.; Zhou, W. Cathode electrochemically reconstructed V-doped CoO nanosheets for enhanced alkaline hydrogen evolution reaction. *Chem. Eng. J.* **2022**, *432*, 134331. [CrossRef]
6. He, D.; Cao, L.; Feng, L.; Li, S.; Feng, Y.; Li, G.; Zhang, Y.; Li, J.; Huang, J. Dual modulation of morphology and electronic structures of VN@C electrocatalyst by W doping for boosting hydrogen evolution reaction. *Chin. Chem. Lett.* **2022**, *33*, 4781–4785. [CrossRef]
7. Yang, J.; Shin, H. Recent advances in layered transition metal dichalcogenides for hydrogen evolution reaction. *J. Mater. Chem. A* **2014**, *2*, 5979–5985. [CrossRef]
8. Chang, B.; Deng, L.; Wang, S.; Shi, D.; Ai, Z.; Jiang, H.; Shao, Y.; Zhang, L.; Shen, J.; Wu, Y.; et al. A vanadium–nickel oxynitride layer for enhanced electrocatalytic nitrogen fixation in neutral media. *J. Mater. Chem. A* **2022**, *8*, 91–96. [CrossRef]
9. Xie, J.; Li, S.; Zhang, X.; Zhang, J.; Wang, R.; Zhang, H.; Pan, B.; Xie, Y. Atomically-thin molybdenum nitride nanosheets with exposed active surface sites for efficient hydrogen evolution. *Chem. Sci.* **2014**, *5*, 4615–4620. [CrossRef]
10. Berenguer, R.; Guerrero-P'erez, M.O.; Guzm'an, I.; Rodríguez-Mirasol, J.; Cordero, T. Synthesis of vanadium oxide nanofibers with variable crystallinity and V^{5+}/V^{4+} ratios. *ACS Omega* **2017**, *2*, 7739–7745. [CrossRef]
11. Zheng, X.; Qin, M.; Ma, S.; Chen, Y.; Ning, H.; Yang, R.; Mao, S.; Wang, Y. Strong Oxide-Support Interaction over IrO_2/V_2O_5 for Efficient pH-Universal Water Splitting. *Adv. Sci.* **2022**, *9*, 2104636. [CrossRef] [PubMed]
12. Dey, K.; Jha, S.; Kumar, A.; Gupta, G.; Srivastava, A.; Ingole, P. Layered vanadium oxide nanofibers as impressive electrocatalyst for hydrogen evolution reaction in acidic medium. *Electrochim. Acta* **2019**, *312*, 89–99. [CrossRef]
13. Khan, Z.; Senthilkumar, B.; Park, S.; Yang, J.; Lee, J.; Song, H.; Kim, Y.; Kwak, S.; Ko, H. Carambola Shaped VO_2 Nanostructures: A Binder–Free Air Electrode for Aqueous Na–Air Battery. *J. Mater. Chem. A* **2017**, *5*, 2037–2044. [CrossRef]
14. Zhang, J.; Zhang, H.; Liu, M.; Xu, Q.; Jiang, H.; Li, C. Cobalt-stabilized oxygen vacancy of V_2O_5 nanosheet arrays with delocalized valence electron for alkaline water splitting. *Chem. Eng. Sci.* **2020**, *227*, 115915. [CrossRef]
15. Choi, Y.-H. VO_2 as a Highly Efficient Electrocatalyst for the Oxygen Evolution Reaction. *Nanomaterials* **2022**, *16*, 939.
16. Ding, Y.; Wen, Y.; Wu, C.; Aken, P.; Maier, J.; Yu, Y. 3D V_6O_{13} Nanotextiles Assembled from Interconnected Nanogrooves as Cathode Materials for High-Energy Lithium Ion Batteries. *Nano Lett.* **2015**, *15*, 1388–1394. [CrossRef]
17. Rao, Y.; Chen, S.; Yue, Q.; Zhang, Y.; Kang, Y. V_2O_3/MnS Arrays as Bifunctional Air Electrode for Long-Lasting and Flexible Rechargeable Zn-Air Batteries. *Small* **2022**, *18*, 2104411. [CrossRef]
18. Liu, Y.; Lv, T.; Wang, H.; Guo, X.; Liu, C.; Pang, H. Nsutite-type VO_2 microcrystals as highly durable cathode materials for aqueous zinc-Ion batteries. *Chem. Eng. J.* **2021**, *417*, 128408. [CrossRef]
19. Fu, S.; Zhu, C.; Song, J.; Engelhard, M.; Du, D.; Lin, Y. Three-dimensional Nitrogen-Doped Reduced Graphene Oxide/Carbon Nanotube Composite Catalysts for Vanadium Flow Batteries. *Electroanalysis* **2017**, *29*, 1469–1473. [CrossRef]
20. Fan, K.; Zou, H.; Duan, L.; Sun, L. Selectively Etching Vanadium Oxide to Modulate Surface Vacancies of Unary Metal–Based Electrocatalysts for High-Performance Water Oxidation. *Adv. Energy Mater.* **2020**, *10*, 1903571. [CrossRef]
21. Xu, H.; Zheng, R.; Du, D.; Ren, L.; Li, R.; Wen, X.; Zhao, C.; Zeng, T.; Zhou, B.; Shu, C. Cationic vanadium vacancy-enriched $V_{2-x}O_5$ on V_2C MXene as superior bifunctional electrocatalysts for Li-O_2 batteries. *Sci. China Mater.* **2022**, *65*, 1761–1770. [CrossRef]

22. Xu, L.; Jiang, Q.; Xiao, Z.; Li, X.; Huo, J.; Wang, S.; Dai, L. Plasma-engraved Co_3O_4 nanosheets with oxygen vacancies and high surface area for the oxygen evolution reaction. *Angew. Chem. Int. Ed.* **2016**, *55*, 5277–5281. [CrossRef] [PubMed]
23. Forner-Cuenca, A.; Biesdorf, J.; Gubler, L.; Kristiansen, P.; Schmidt, T.; Boillat, P. Engineered water highways in fuel cells: Radiation grafting of gas diffusion layers. *Adv. Mater.* **2015**, *27*, 6317–6322. [CrossRef]
24. Song, F.; Hu, X. Exfoliation of layered double hydroxides for enhanced oxygen evolution catalysis. *Nat. Commun.* **2014**, *5*, 4477. [CrossRef] [PubMed]
25. He, D.; Cao, L.; Huang, J.; Kajiyoshi, K.; Wu, J.; Wang, C.; Liu, Q.; Yang, D.; Feng, L. In-situ optimizing the valence configuration of vanadium sites in NiV-LDH nanosheet arrays for enhanced hydrogen evolution reaction. *J. Energy Chem.* **2020**, *47*, 263–271. [CrossRef]
26. Xue, Z.; Su, H.; Yu, Q.; Zhang, B.; Wang, H.; Li, X.; Chen, J. Janus Co/CoP nanoparticles as efficient motte-Schottky electrocatalysts for overall water splitting in wide pH range. *Adv. Energy. Mater.* **2017**, *7*, 1602355. [CrossRef]
27. Zhang, J.; Wang, T.; Pohl, D.; Rellinghaus, B.; Dong, R.; Liu, S.; Zhuang, X.; Feng, X. Interface engineering of MoS_2/Ni_3S_2 heterostructures for highly enhanced electrochemical overall-water-splitting activity. *Angew. Chem. Int. Ed.* **2016**, *55*, 6702–6707. [CrossRef]
28. Wang, Q.; Zhao, Z.; Dong, S.; He, D.; Lawrence, M.; Han, S.; Cai, C.; Xiang, S.; Rodriguez, P.; Xiang, B.; et al. Design of active nickel single-atom decorated MoS_2 as a pH-universal catalyst for hydrogen evolution reaction. *Nano Energy* **2018**, *53*, 458–467. [CrossRef]
29. Rao, Y.; Zhang, L.; Shang, X.; Dong, B.; Liu, Y.; Lu, S.; Chi, J.; Chai, Y.; Liu, C. Vanadium sulfides interwoven nanoflowers based on in-situ sulfurization of vanadium oxides octahedron on nickel foam for efficient hydrogen evolution. *Appl. Surf. Sci.* **2017**, *423*, 1090–1096. [CrossRef]
30. Chalotra, S.; Mir, R.; Kaur, G.; Pandey, O. Oxygen deficient V_2O_3: A stable and efficient electrocatalyst for HER and high performance EDLCs. *Ceram. Int.* **2020**, *46*, 17954–17962. [CrossRef]
31. Xie, Z.; Wang, W.; Ding, D.; Zou, Y.; Cui, Y.; Xu, L.; Jiang, J. Accelerating Hydrogen Evolution at Neutral pH by Destabilization Water with Conducting Oxophilic Metal Oxide. *J. Mater. Chem. A* **2020**, *8*, 12169–12176. [CrossRef]
32. Zhou, P.; Lv, X.; Gao, Y.; Cui, Z.; Liu, Y.; Wang, Z.; Wang, P.; Zheng, Z.; Dai, Y.; Huang, B. Enhanced electrocatalytic HER performance of non-noble metal nickel by introduction of divanadium trioxide. *Electrochim. Acta* **2019**, *320*, 134535. [CrossRef]
33. Zhou, J.; Xiao, H.; Weng, W.; Gu, G.; Xiao, W. Interfacial confinement of Ni-V_2O_3 in molten salts for enhanced electrocatalytic hydrogen evolution. *J. Energy Chem.* **2020**, *50*, 280–285. [CrossRef]
34. Yang, Y.; Yao, H.; Yu, Z.; Islam, S.; He, H.; Yuan, M.; Yue, Y.; Xu, K.; Hao, W.; Sun, G.; et al. Hierarchical Nanoassembly of $MoS_2/Co_9S_8/Ni_3S_2/Ni$ as a Highly Efficient Electrocatalyst for Overall Water Splitting in a Wide pH Range. *J. Am. Chem. Soc.* **2019**, *141*, 10417–10430. [CrossRef] [PubMed]
35. Kou, T.; Smart, T.; Yao, B.; Chen, I.; Thota, D.; Ping, Y.; Li, Y. Theoretical and experimental insight into the effect of nitrogen doping on hydrogen evolution activity of Ni_3S_2 in alkaline medium. *Adv. Energy Mater.* **2018**, *8*, 703538.
36. Niu, Y.; Li, W.; Wu, X.; Feng, B.; Yu, Y.; Hu, W.; Li, C. Amorphous nickel sulfide nanosheets with embedded vanadium oxide nanocrystals on nickel foam for efficient electrochemical water oxidation. *J. Mater. Chem. A* **2019**, *7*, 10534–10542. [CrossRef]